

Drosophila Visual System Inspired Ambipolar OFET for Motion Detection

Tao Xie, Yan-Bing Leng, Tao Sun, Shirui Zhu, Hecheng Cai, Pengfei Han, Yu-Qi Zhang, Jingrun Qin, Runze Xu, Zezhuang Yi, Ye Zhou, and Su-Ting Han*

Drosophila can rapidly and precisely detect changes in light in their surroundings and achieve acute perception of motion information with high energy efficiency and adaptivity owing to the cooperation of “ON” channel and the “OFF” channel in its visual system. Optical controlled bidirectional synaptic behavior of neuromorphic device is important for modeling parallel processing channels of Drosophila’s visual system. In this study, an ambipolar transistor utilizing a bilayer architecture composed of p-type pentacene and n-type C₆₀ as semiconductors is developed, with near-infrared (NIR) PbS quantum dots serving as the charge-trapping layer. This design enables a gate-tunable positive and negative photoresponse, driven by photogating and photovoltaic effects at visible and NIR wavelengths. When regulated by a negative gate voltage, the device exhibits a suppressed photocurrent relaxation time exceeding 1000 s, demonstrating stable long-term inhibitory characteristics. Consequently, high-contrast excitatory and inhibitory synapses facilitate orientation and motion detection. Identification accuracies of up to 94.8% for motion direction and 98.1% for dynamic gestures are achieved. Practical applications such as intelligent monitoring and human–computer interaction stand to benefit significantly from these findings.

robotics, and artificial intelligence become more prevalent, current image sensors encounter significant challenges.^[2–6] Even with the advancement of algorithms specifically designed for these open-world scenarios, image sensors struggle to manage dynamic, diverse, and unpredictable edge cases that fall outside their sensing capabilities, leading to algorithm failures.^[7–9] Traditional sensors experience increased power and bandwidth demands as they achieve higher spatial resolution, speed, and precision. This results in limited capture capabilities and an overwhelming amount of data.^[10–12]

In contrast to existing image sensors, the biological visual system is distinguished by its versatility, adaptability, and robustness in open-world environments.^[3,13–15] Biological-visual systems possess distinct advantages in the processing of visual information as compared to traditional machine vision systems.^[16,17] For instance, the compound visual system exhibits high motion sensitivity and large visual field

1. Introduction

Image sensors are integral to a wide array of applications.^[1] However, as open-world applications like autonomous machines,

range.^[13,18–21] The compound eye processes motion visual information through two parallel channels: the “ON” channel and the “OFF” channel.^[22–24] Drosophila can rapidly and precisely detect changes in light in their surroundings and achieve acute perception of motion information with the cooperation of these two pathways, which have excitatory and inhibitory functions in the visual system, respectively.^[22,25] **Figure 1a** schematically illustrates the parallel channels found in the Drosophila compound eye, which includes the retina and visual ganglia. The visual ganglia consist of four successive neuronal layers: lamina, medulla, lobula, and lobula plate.^[26–29] After being detected by photoreceptors in the retina, visual information is sent to the lamina for additional processing.^[27,30] L1 and L2 neurons in the lamina are in charge of identifying the boundaries of brightness and darkness in moving objects, respectively. These neurons provide the input signals for the “ON” and “OFF” pathways.^[22,25,31] The signal is processed by medullary neurons and then passed on to the lobula and lobula plate.^[29] Lobula and lobula plate can be categorized as a lobular complex, in which motion-detecting neurons show a highly dense distribution.^[32–34] T4 and T5 cells in the lobular complex are the primary candidates to process signals from “ON” and “OFF” motion pathways, respectively, and to detect motion.^[35–37] Different subtypes of T4 and T5 cells play

T. Xie, T. Sun, Y.-Q. Zhang, J. Qin, R. Xu
Institute of Microscale Optoelectronics
Shenzhen University
Shenzhen 518060, P. R. China

Y.-B. Leng, S. Zhu, S.-T. Han
Department of Applied Biology and Chemical Technology
The Hong Kong Polytechnic University
Kowloon, Hong Kong 999077, P. R. China
E-mail: suting.han@polyu.edu.hk

H. Cai, P. Han, Z. Yi
College of Electronics and Information Engineering
Shenzhen University
Shenzhen 518060, P. R. China

Y. Zhou
Institute for Advanced Study
Shenzhen University
Shenzhen 518060, P. R. China

The ORCID identification number(s) for the author(s) of this article can be found under <https://doi.org/10.1002/adfm.202415457>

DOI: 10.1002/adfm.202415457

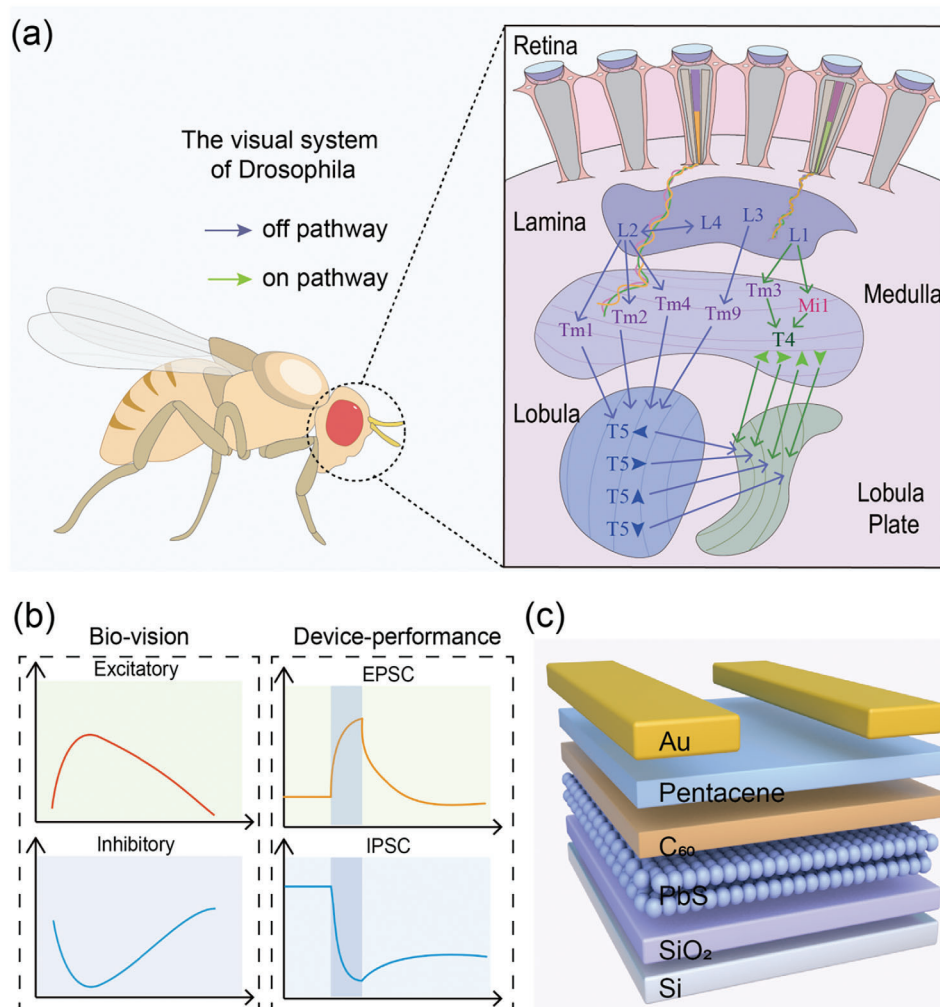


Figure 1. Bidirectional light-responsive synaptic devices inspired by the functional principles observed in insect compound eyes. a) The structure of the *Drosophila* compound eye visual system. b) Biological synaptic plasticity (excitation and inhibition) in the *Drosophila* visual system and synaptic device performance (EPSC and IPSC). c) The structure diagram of a PbS/C₆₀/Pentacene bipolar transistor.

distinct roles in visuomotor coding. Specifically, subtypes a and b specialize in the encoding of horizontal motion information, whereas subtypes c and d focus on the encoding of vertical motion information.^[38,39] T4 and T5 neurons are able to receive input signals from a variety of different receptive fields and produce membrane potentials that represent the motion dynamics of objects in the visual field, allowing neural networks to detect motion precisely. Neuromorphic devices are often used to simulate biological retinal behavior due to their tunable volatility and complex dynamics. For example, simulation of photoreceptors converts external light stimuli into electrical signals through photo-electronic conversion, thus enabling optical information sensing, memory, color recognition, and visual adaptation.^[40–44] Simulation of ganglion cell transfers direction, shape, color, size, contrast, and other optical information.^[45] Simulation of horizontal cells and amacrine cells suppress the received useless information to improve image contrast.^[46,47] However, most of them focus on single-channel processing of visual information. Compared with a single “ON” channel, the “ON” / “OFF” parallel pro-

cessing channels of the *Drosophila* vision system have significant advantages in processing visual information^[22–24,48]: 1) Energy efficiency, the “ON” and “OFF” pathways in the visual system manage changes in light and darkness, respectively. When processing images, this distinction enables the system to achieve a more effective energy allocation. 2) Adaptability, the system may adjust more effectively to various workloads and surroundings thanks to the “ON” and “OFF” channel processing. In bright conditions, the “ON” path may be activated more frequently, and in dark environments, the “OFF” path may be activated more frequently.^[49] 3) Complexity: Processing the “ON” and “OFF” pathways increases the system’s complexity and may help it perform more difficult visual tasks.

Optical controlled bidirectional synaptic behavior of neuromorphic device is important for modeling parallel processing channels of *Drosophila*’s visual system (Figure 1b).^[50–52] On the one hand, bidirectional synaptic plasticity allows reversible information processing during behavioral learning updates.^[53,54] On the other hand, bidirectional adjustment of synaptic weights is

capable to increase the contrast between the target object and the surroundings, thereby speeding up image processing and improving recognition accuracy.^[55–57]

Ambipolar transistors show great potential for achieving bidirectional photosynaptic properties due to their unique type of bipolar carriers and their ability to regulate the gate voltage nonlinearly.^[58–61] Pentacene, as a P-type organic semiconductor material, can effectively transport holes with high hole mobility. Its ordered molecule structure is composed of five parallel benzene rings, ensuring its excellent stability. Similarly, C₆₀ is commonly used in the manufacture of N-type organic transistors owing to its satisfied electron transport characteristics. The strong π – π interaction between C₆₀ molecules makes the carrier transport efficiently, results a high carrier mobility. The heterojunction interface formed by pentacene and C₆₀ helps to effectively separate photogenerated electron–hole pairs and improve the photoelectric conversion efficiency by sequentially depositing materials using evaporation technology. In addition, the pentacene/C₆₀ heterogeneous structure has a wide spectral response range and perceives external information in the visible band. However, the perception of near-infrared (NIR) information also became an important technology for various potential applications, such as fiber optic communications, medical imaging/diagnostics, and revealing potential risks at night. PbS quantum dots (QDs) possess the ability to extend the perception of devices beyond the visible spectrum to NIR band. Moreover, solution processing and its reasonable price make it suitable for large-scale manufacturing, further expanding flexible and wearable application scenarios.

Here, we constructed an ambipolar transistor based on the bilayer architecture of p-type pentacene and n-type C₆₀ as semiconductor and NIR PbS QDs as charge trapping layer. The gate-tunable positive and negative photoresponse is achievable stemming from the photogating and photovoltaic effect at visible and NIR wavelengths. Under the regulation of the negative gate voltage, the relaxation time of the suppressed photocurrent of the device can reach more than 1000 s, showing a stable long-term inhibitory characteristic. Thus, orientation detection and motion detection are achieved by high contrast excitatory and inhibitory synapses. For both motion direction and dynamic gestures, we were able to achieve identification accuracy of up to 94.8% and 98.1%, respectively. Together with fostering the deep integration of machine learning algorithms and optoelectronic devices, this research opens up new avenues for technical exploration and provides a broad development space for related fields of study. Practical applications such as intelligent monitoring and human-computer interaction benefit from these discoveries.

2. Results and Discussion

2.1. Design of Organic Heterojunction Transistor

Figure 2a and **Figure S1** (Supporting Information) illustrate the schematic illustration of an organic field effect transistor (OFET) device with a vertical structure, displaying its 3D arrangement. Hole trapping layers are composed of PbS QDs, semiconductor layers are composed of Pentacene and C₆₀, and top sources and drains are coated with Au. The detailed fabrication steps can be found in the experimental section. The OFET devices

based on PbS QDs films and organic heterojunctions exhibit ambipolar transport characteristics with V-shaped transfer curves, as shown in **Figure 2b**. Furthermore, the OFET possesses a wide range of optical responses from the visible to the NIR region owing to the wide absorption band of PbS QDs and pentacene/C₆₀ heterostructure (**Figure 2c**). **Figure S2** (Supporting Information) displays the PbS QDs dispersion with concentration of 0.05 mg mL^{−1}, and **Figure S3** (Supporting Information) displays the atomic force microscopy (AFM) image of the surface morphology of the organic films. Scanning electron microscope (SEM) technology was used to characterize the distribution of PbS QDs on the film surface (**Figure S4**, Supporting Information). As presented, the PbS QDs solution is uniformly distributed, ensuring that spin-coating techniques can produce homogeneously distributed trapping sites on the SiO₂ substrate. Also, the average surface roughness of pentacene films developed on C₆₀ films is merely 6.74 nm. This suggests that organic films produced using thermal vapor deposition exhibit great flatness, which serves as a foundation for achieving balanced ambipolar behavior.

2.2. Linearly Gate-Tunable Bidirectional Photosynaptic Properties

In the field of neuroscience, the electrical activity produced by a presynaptic neuron is transformed into neurotransmitters, which then attach to specific receptors located on postsynaptic terminals.^[62–64] This binding activity subsequently initiates a modification in the postsynaptic current. Specifically, excitatory postsynaptic current (EPSC) is resulted from the postsynaptic activation of excitatory neurotransmitters like glutamate. As opposed to this, inhibitory neurotransmitters, such as gamma-aminobutyric acid, cause an inhibitory action, resulting in an inhibitory postsynaptic current (IPSC). Similar to biological synapses, photosynaptic devices utilize the light signal as a feed-forward stimulus, and the output current of the channel is considered a postsynaptic current.^[65–67] Different modulations of the device's conductance can be achieved by changing the conditions of the stimulus. Furthermore, for ambipolar transistors, nonlinear modulation of the gate voltage dramatically expands the device's conductivity state.^[58,60,68,69] This nonlinear modulation allows the transistor to exhibit variable conductance properties in a variety of light pulse situations. To investigate the optical synaptic performance of the OFET, the photoresponse characteristics were tested at different gate voltages and different wavelengths (wavelengths: 458/519/637/980 nm, pulse width: 0.5 s, optical power: 4.8 μ W cm^{−2}) as shown in **Figure 2d**. When $V_g > 0$, the FET demonstrates the negative photoconductivity (NPC) effect, the current level under optical pulse is lower than the starting current level. In contrast, when $V_g < 0$, the FET exhibits the positive photoconductivity effect, resulting in a substantial increase in the current level under optical pulse (**Figure 2e**). In order to facilitate explanation, our subsequent performance investigation primarily concentrated on the optical response characteristics of 458 nm.

Figure 2f illustrates the change in the photocurrent value of the device for varied pulse width (0.125, 0.25, 0.5, 1, and 1.25 s) while maintaining a gate voltage of 5 V and −8 V. When the gate voltage is 5 V, the device's channel current rises rapidly due to

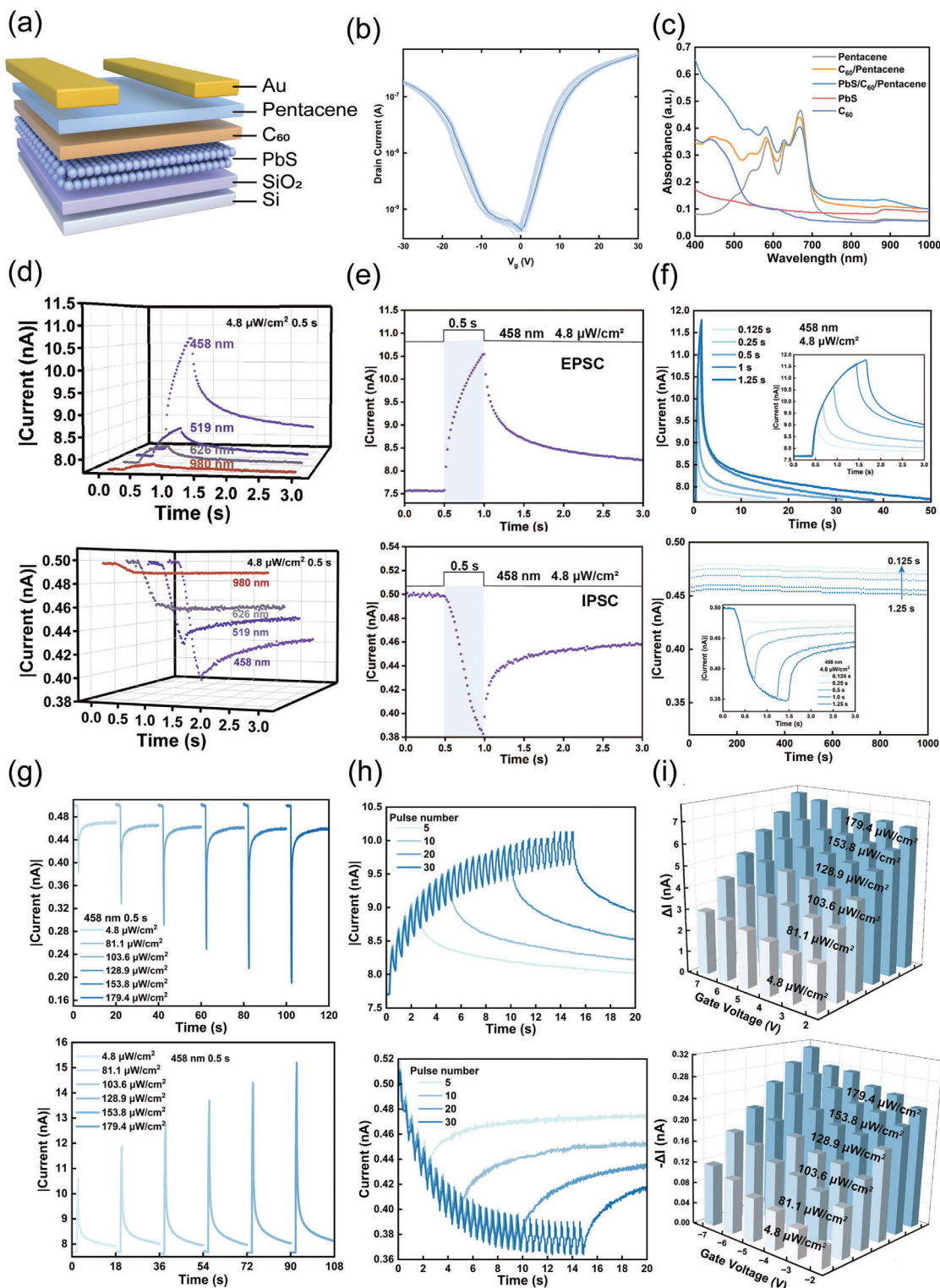


Figure 2. Characterization of optoelectronic properties and bidirectional optoelectronic synaptic behavior of the OFET. a) The schematic of an OFET device with a vertical structure. b) Transfer curves of the OFET devices in dark condition. c) Absorption spectra of different material combinations. d) Bidirectional photoresponse characteristics of the device under different light wavelength conditions: $V_g = 5$ V (top); $V_g = -8$ V (bottom). e) Bidirectional photoresponse characteristics of the device at 458 nm light wavelength: $V_g = 5$ V (top) (EPSC); $V_g = -8$ V (bottom) (IPSC). f) The time-plasticity of the device under different gate voltage regulation: $V_g = 5$ V (top); $V_g = -8$ V (bottom). g) The effect of optical pulse amplitude on the device bidirectional synaptic plasticity: $V_g = 5$ V (top); $V_g = -8$ V (bottom). h) The effect of the number of light pulses on the bi-directional synaptic plasticity of the device: $V_g = 5$ V (top); $V_g = -8$ V (bottom). i) Modulation of gate voltage for photosynaptic weights.

photogenerated electrons. The injection of photogenerated electrons into the channel is interrupted when the optical signal is withdrawn, causing the holes and electrons to gradually combine and the current to decay. This decay is relatively rapid at the beginning, but slows down with eclipse of time. The photocurrent relaxation time increases from the initial 15 to 50 s with the change in illumination time, achieving the transition from short-term potentiation (STP) to long-term potentiation (LTP). When the gate voltage is -8 V, the light stimulation induces the trapping of photogenerated holes in the PbS layer and the photogenerated electrons are swept into the channel to decrease the device conductance. Furthermore, the conductance of the device is always lower after the withdrawal of the optical signal. Inhibitory photoresponse of this device shows longer relaxation times than 1000 s. As shown in Figure 2g, the photocurrent value of the device is directly related to the optical pulse amplitude. When a positive gate voltage is applied, the absolute value of current increases from 11 nA ($4.8 \mu\text{W cm}^{-2}$) to 15.2 nA ($179.4 \mu\text{W cm}^{-2}$). Conversely, when a negative gate voltage is applied, the current value is reduced from 0.38 nA ($4.8 \mu\text{W cm}^{-2}$) to 0.18 nA ($179.4 \mu\text{W cm}^{-2}$) in response to the light pulse. The greater the amplitude of the light pulse (the higher the optical power), the more significant the impact of light-induced learning. As the pulse amplitude increases, the rate at which the photocurrent grows gradually decreases, and the device's learning ability approaches saturation. Figure 2h illustrates the variations in synaptic weights of the OFET when exposed to various amounts of light pulses (5/10/20/30 light pulses). The increase in the number of light pulses induces more pronounced photoenhancement and photosuppression characteristics, resulting in the transition from a state of STP (STD) to LTP (LTD). Specifically, increasing the gate voltage can effectively promote the generation and separation efficiency of photogenerated carriers, which in turn significantly enhances the conductivity of the transistor. To accurately quantify this phenomenon, the various photocurrent value (ΔI) is introduced, defined as the absolute difference between the leakage current measured under constant illumination conditions (I_{light}) and that recorded in the absence of illumination (I_{dark}), represented by $\Delta I = |I_{\text{light}}| - |I_{\text{dark}}|$. The figure of the magnitude of the varying current value versus gate voltage (Figure 2i) shows that the OFET has a bi-directional photoresponse characteristic with adjustable gate voltage. Furthermore, the prepared OFET demonstrates consistent bidirectional photoresponse characteristics when subjected to other wavelength stimuli (Figures S5–S7, Supporting Information). Stable bidirectional optical synaptic properties are an important prerequisite for simulating the antagonistic function of the parallel processing pathway of the compound eye. In addition, power consumption is also a significant parameter to characterize the phototransistor. The power consumption is defined as $E = V_{\text{DS}} \times I_{\text{EPSC}} \times t$, where V_{DS} , I_{EPSC} , t represent reading voltage, EPSC maximum current, and duration of light pulse, respectively. As shown in Figure S8 (Supporting Information), a light pulse width of 100 ms still allows the device to generate an effective EPSC, while the power consumption is as low as 5.7 fJ, which is in the power consumption range per pulse of biological synapses (1–100 fJ). We also compare the performance of our device with other neuromorphic devices that simulate the function of biological vision systems, Table S1 (Supporting Information) details the results. Our device exhibited abun-

dant synaptic behavior, wide optical signal perception range, and low consumption power, indicating its potential for future intelligent perception and human-computer interaction systems.

2.3. Mechanism of Operation of Bidirectional Photosynaptic Properties

Specifically, the device functions primarily in the electron accumulation mode when $V_{\text{g}} > 0$ V (Figure 3a). In this mode, electrons are effectively gathered and transported as dominant charge carriers within the C_{60} layer. The semiconductor layer absorbs light energy and generates electron-hole pairs. Due to the internal electric field, the electron-hole pairs separate at the interface of the PN junction. The photogenerated electrons increase the number of carriers in the channel, resulting in enhancement of device conductivity. Upon cessation of the light stimulation, the photogenerated electrons and holes recombine, resulting in the transition back to original conductance. In contrast, when $V_{\text{g}} < 0$ V (Figure 3b), holes become dominant charge carriers and accumulate and transport within the top Pentacene layer. The PbS film captures the holes formed by light, while the electrons generated by light form complexes with the holes in the channel, resulting in a decrease in the conductance of the device.^[70–72] Furthermore, the current suppression effect will be sustained for a considerable amount of time since it is difficult for the trapped holes to re-enter the channel through the C_{60} layer following the removal of the light stimulation. So, as shown in Figure 3c, when the light pulse hits the device, the transmission characteristic curve moves to the left, and there is a clear decrease in hole transport in the area of negative gate voltage.

Only excitatory photosynaptic behaviors can be observed for C_{60} /pentacene FET device (Figure S9, Supporting Information), which indicates the PbS film is essential to realize bidirectional optoelectronic synapses. In order to explore the effect of insulating oleic acid ligands on device, we used oleic acid instead of the original PbS QDs layer to investigate its effect on device performance (Figure S10, Supporting Information). The results further verify PbS QDs is crucial for in NIR light response behavior and NPC behavior. In addition, Kelvin probe force microscopy (KPFM) was used to investigate the surface potential of the FET under both dark and light conditions. The results demonstrated a gradual decrease in surface potential in response to light stimulation, with a more significant decrease observed at shorter wavelengths (from 746 mV (dark conditions) to 529 mV (458 nm)) (Figure 3d). This finding provides further evidence for the presence of a hole-trapping effect.

2.4. Orientation Recognition System Based on Bionic Parallel Processing Pathways

2.4.1. Orientation Recognition Based on OFET Time-Coded Characteristics

To assess visual motion, *Drosophila* integrates spatial and temporal light intensity data. Because nonlinear processing is needed for this integration, motion-estimating circuits are sensitive to particular spatiotemporal correlations that represent visual

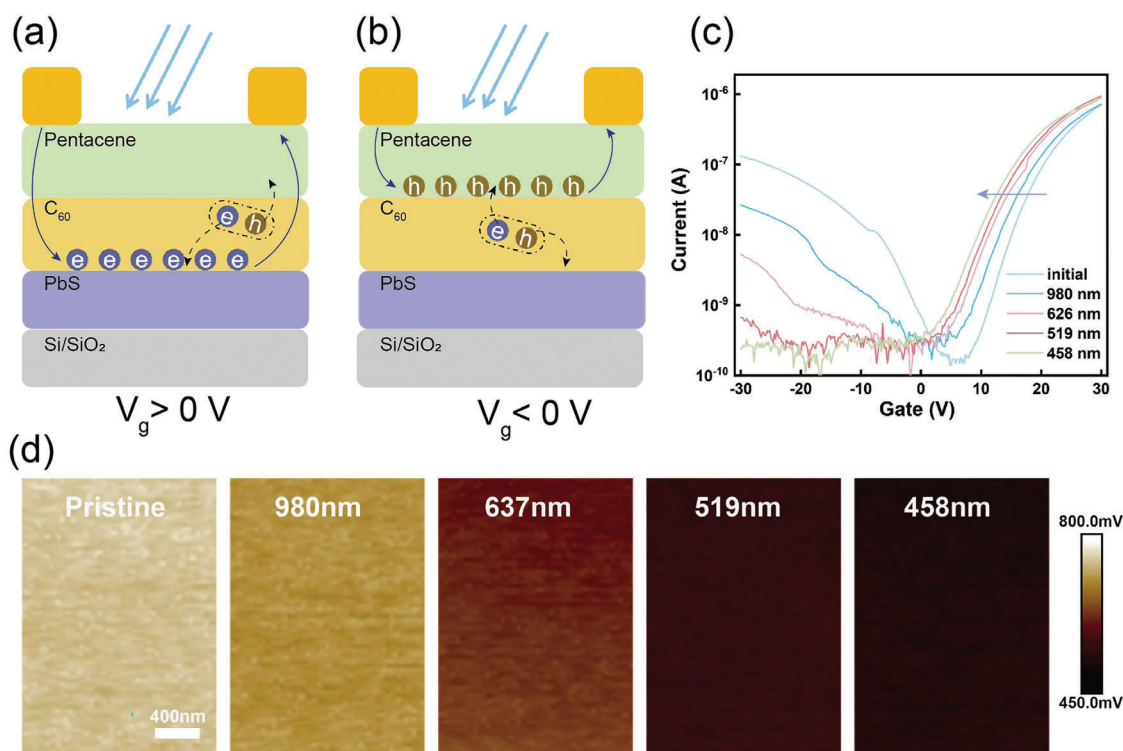


Figure 3. Mechanistic explanation of the bidirectional photosynaptic properties. a,b) Schematic diagram of the operating mechanism of OFET devices at $V_g > 0$ and $V_g < 0$. c) Transfer characteristic curves at different light wavelengths. d) The variation of surface potential of devices under different light wavelengths.

motion.^[33,35,73,74] These correlations are weighted by classical models of motion estimation (EDM models) to provide direction-selective signals.^[37,75,76] As an image passes through a photoreceptor field, it produces spatial and temporal light intensity correlations.^[77,78] These correlations provide data that can be used to ascertain the direction and velocity of picture motion. This has not only given *Drosophila* the capacity to quickly capture and interpret motion data in challenging environments, but it has also served as an inspiration for the development of contemporary visual processing systems.

In order to develop a direction recognition system, it was necessary to analyze and test the temporal transactional coding characteristics of the OFET. Four successive optical pulse sequences were used to study its optical reaction. The illustration in Figure 3a depicts a standard “1001” encoding procedure that demonstrates gradual changes at four important time point. This coding system encodes and transmits data by representing various bits of information by the presence or absence of light pulses. The numbers “1” and “0” in this coding scheme stand for light conditions ($28.8 \mu\text{W cm}^{-2}$, 0.2 s) and dark conditions. In the Figure 4a, the organic ambipolar transistor exhibits different response characteristics (ΔI_{ds}) for different four-frame actions under optical stimuli with a width of 0.2 and a 0.2 s interval. This finding reveals that the device is capable of producing distinguishable outputs depending on the order and time interval of the optical stimuli. When the time interval between the two light pulses indicating “1” is much less than a specific threshold value t_0 , the photogenerated carriers of the device will accu-

mulate and increase, thus presenting a larger photocurrent result. On the contrary, when the two “1” stimulus pulses are separated in the time domain (i.e., the time interval is greater than t_0), the ΔI_{ds} output is relatively low due to the release process of the trapped holes. This distinguishable output characteristic suggests that the OFET has the potential to enable time-based transactional coding.

An orientation recognition system was constructed based on two OFET arrays, each containing 20×20 pixel units (Figure 4b). The prepared arrays exhibit a certain degree of electrical and optical performance homogeneity (Figures S11–S13, Supporting Information). These two arrays simulate the information functions of the “ON” and “OFF” channels of the visual system of compound eye, respectively, and they are able to encode spatiotemporal visual information and display the contours of motion trajectories in the visual field, thus enabling the perception of dynamic motion. Figure 4c depicts the implementation flow of the whole function in detail: first, in the time dimension, the driving process of the car is precisely divided into four consecutive frames, each of which captures the position and dynamic state of the car at different points in time. The four image frames are further extracted and encoded into optical pulse signals. Detecting and responding to changes in the light pulse signals is then performed by two optical sensor arrays. Ultimately, a composite output is obtained by superimposing the output signals of these two arrays. This composite signal not only contains information about the car’s position at each point in time, but also reveals information about its trajectory profile and direction.

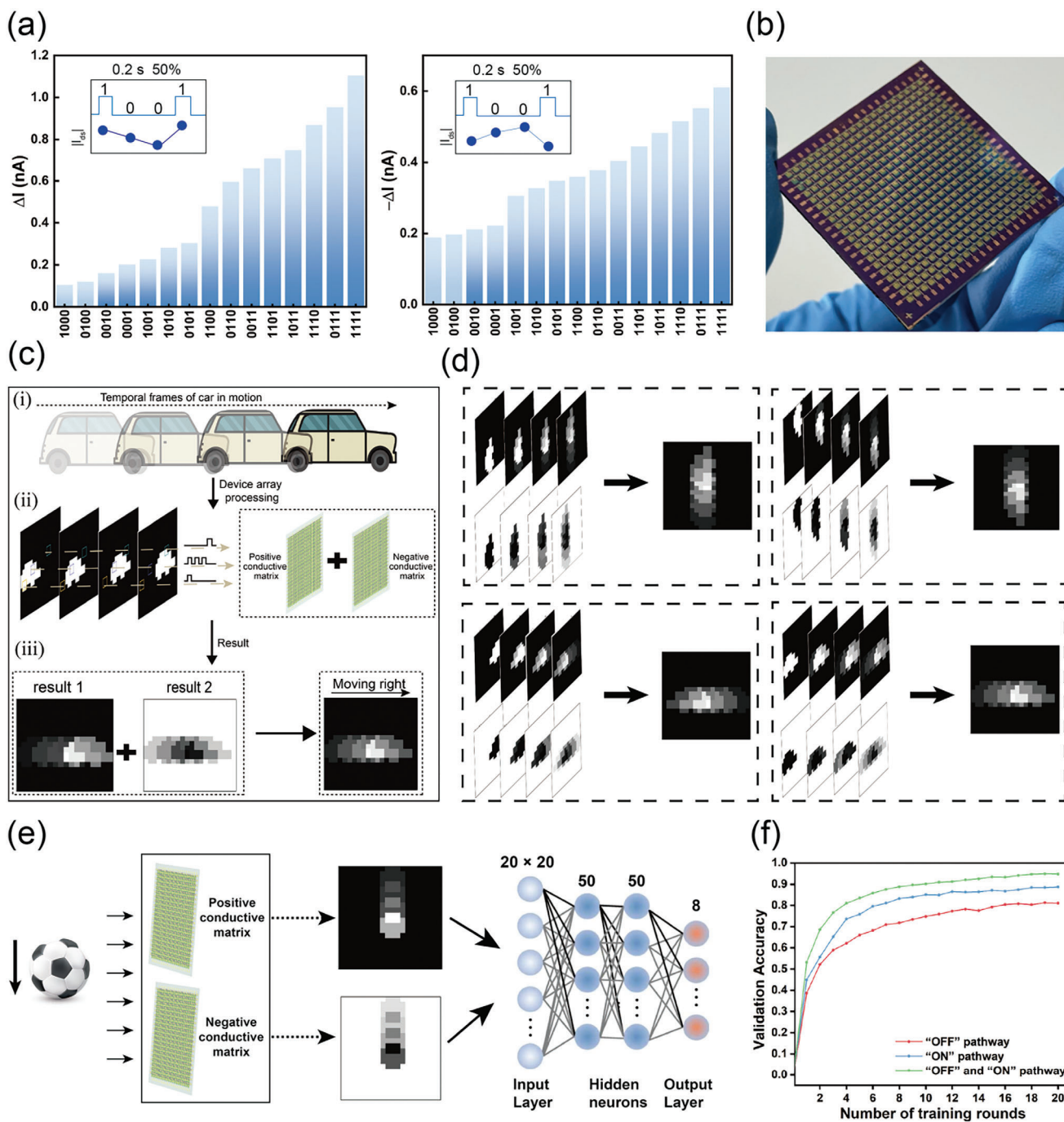


Figure 4. Orientation recognition task based on the OFET of bidirectional optical synaptic properties. a) The time coding characteristics of organic bipolar transistors are: a) the change of device current when the positive gate voltage is adjusted ($V_g = 3$ V), and b) the change of device current when the negative gate voltage is adjusted ($V_g = -15$ V). b) Physical diagram of a 20 × 20 device array. c) Implementation process of direction identification based on two organic bipolar transistor arrays. d) Four basic directions identification results based on organic bipolar transistor arrays. Arrow left: output results of transistor arrays with positive gate voltage regulation (top). output results of transistor arrays with negative gate voltage regulation (bottom). Arrow right: dual-channel processing results. e) Orientation recognition and classification system with Drosophila parallel processing channel functionality. f) Orientation recognition accuracy for different processing channels.

Identifying and analyzing the four fundamental directions of motion—up, down, left, and right—was necessary to completely confirm the viability and stability of the system. Under positive gate voltage modulation, the gadget exhibits a substantially better optical response than it does under negative gate voltage modulation. This means that, in a single-channel output comparison, as Figure 4d illustrates, the positive gate voltage-controlled array outperforms the negative gate voltage-regulated array in terms of motion recognition. After carefully comparing the outputs of various channel combinations, we find that the combined output of two channels performs significantly better than that of a single channel, further proving the bionic and logical nature of the system design. This finding is consistent with the performance of the *Drosophila* vision system.

2.4.2. Orientation Recognition Task Based on Artificial Neural Network (ANN)

High-precision motion orientation recognition is pivotal in the field of machine vision. Its importance is especially significant in application scenarios such as automated vehicle navigation and intelligent surveillance systems.^[52,79,80] To achieve this goal, a bio-inspired in-sensor motion sensing method is employed, drawing on biological principles, to accurately classify the direction of motion of targets such as cars and balls. Bio-inspired visual sensing cleverly fuses a series of image frames with spatiotemporal information into a single compressed image, analogous to the function of the four layers of the optic lobes in the *Drosophila* retina, which enables efficient encoding of dynamic scenes. Meanwhile, the introduction of two transistor arrays controlled by different gate voltages further mimics the functions of the “ON” and “OFF” channels in the *Drosophila* visual system, which enables the system to sense and process motion signals more accurately and comprehensively. As illustrated in Figure 4e, two parallel OFET arrays are sequentially given a series of optical input signals in the form of $X(t)$; one array is driven by a positive gate voltage, while the other is driven by a negative gate voltage. Each pixel point (an OFET) P_n is stimulated by light, and the conductivity changes to form a conducting state, i.e., the network state $U(t)$. At the end of the stimulated signal, the device outputs a fixed-weight current, i.e., the network output $Y(t)$. These output signals are then transmitted to the ANN for further recognition and classification, allowing for the detection of different objects' motion directions. A specialized dataset was created for this experiment, encompassing four distinct sorts of actual motion patterns exhibited by the ball and the cat: upward, downward, leftward, and rightward. In each scenario, we designated a training set consisting of 1000 photos (totaling 8000 image frames) and a test set including 300 samples (totaling 2400 image frames) to assess the accuracy of the proposed orientation identification system. As shown in Figure 4f, during a 20-training cycle period consisting of 1000 iterations, the two-channel processing method demonstrates a recognition accuracy of approximately 94.8%. This represents a notable enhancement when compared to the 88.7% recognition accuracy achieved by the “ON” processing channel (regulated by a positive gate voltage-transistor array) and the 80.0% recognition accuracy of the “OFF” processing channel (regulated by a negative gate voltage-transistor array).

2.5. Dynamic Gesture Recognition Task Based on Bionic Parallel Processing Pathways

2.5.1. A Preprocessing System for Extracting Motion Objects

When studying situations where motion is detected in the real world, it is important to consider the background information. This information is frequently very noticeable and takes up a significant portion of the visual scene. The intricate nature of background information presents a significant obstacle to motion detection, necessitating the use of algorithms and approaches that can precisely differentiate and identify the distinction between a moving target and a stationary background.^[81,82] In *Drosophila* species, the processing of different brightness change information through “ON” and “OFF” channels enables the extraction and tracking of moving targets. A preprocessing system for extracting motion objects is constructed based on the motion information processing mechanism of *Drosophila*. The system network comprises two parallel modules, each consisting of $N \times M$ pixels (OFETs). The values of N and M are determined by the image resolution, representing the length and width of the image, respectively. And, the two sets of pixel modules exhibit the response characteristics of EPSC and IPSC, respectively. As shown in Figure 5a, taking the scene of a boy playing basketball as an example, the full motion process can be regarded as a series of image sequences with temporal characteristics, the image information from the moments from 0 to t_1 is sequentially encoded as optical information and inputted into the constructed parallel pixel module. When this spatiotemporal information is input in the form of an optical signal $X(t)$, the dynamic storage layer $U(t)$ of the system is obtained by matrix multiplication of $X(t)$ with the optical response of the transistor matrix. Therefore, $U(t)$ is dynamically adjusted in response to the input signal $X(t)$. At the moment $t_0 + \Delta t$, the output signal $O(t_0 + \Delta t)$ is obtained by normalizing the dynamic storage layer difference (i.e., $|U(t_0 + \Delta t) - U(t_0)|$), which effectively identifies the moving object in the dynamic information. If there is no moving object in the t_0 time period (i.e., static information flow) and no new optical signal is input to the corresponding pixel module at the time $t_0 + \Delta t$, then the values of $U(t_0 + \Delta t)$ and $U(t_0)$ are similar. Therefore, $O(t_0 + \Delta t)$ is close to zero, which is regarded as static noise and filtered out by the system. On the contrary, if there is a moving object (i.e., a dynamic information stream), the output signal $O(t_0 + \Delta t)$ will obtain a positive value, and thus the moving object will be detected. Figure 5b compares the output values of a stationary object (a basketball hoop) and a moving object (a boy and a basketball). The output values of the stationary objects fluctuate less, but they are both close to 0. In contrast, moving objects present a sharp and dynamic output over time. This processing provides us with an effective tool to easily and accurately extract the moving objects from the stationary background based on the apparent difference in output values.

2.5.2. Dynamic Gesture Recognition Task

The raw video input, also known as the unprocessed information stream, contains a wealth of varied information. In addition to the dynamic object data necessary for action recognition, this

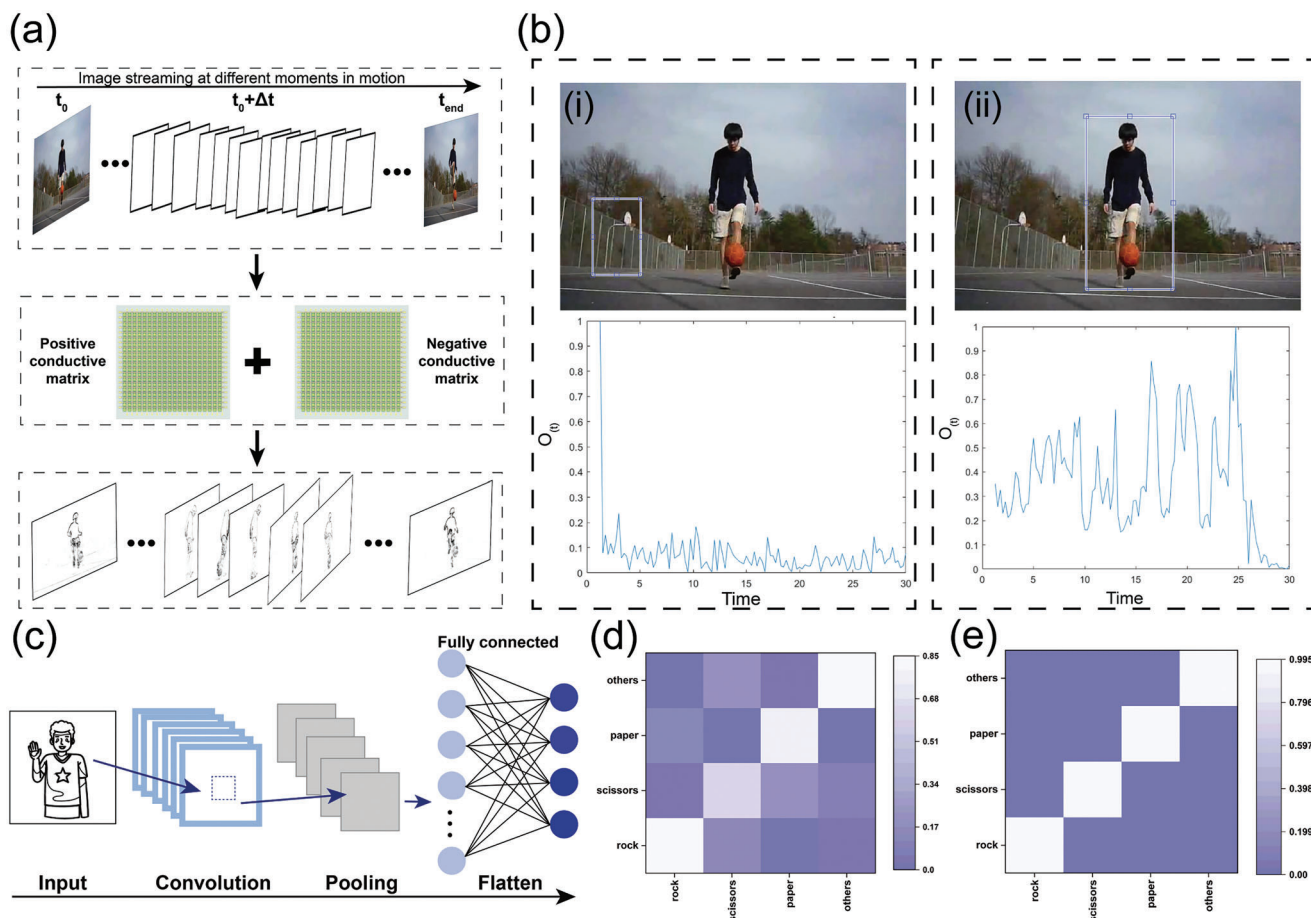


Figure 5. Dynamic gesture recognition task based on the OFET of bidirectional optical synaptic properties. a) Schematic diagram of the motion target extraction process based on the bidirectional optical synaptic properties of the OFET arrays. b) Motion object extraction results: stationary objects and its output value changes (left); moving objects and its output value changes (right). c) Schematic of motion detection system combining motion object extraction system and CNN. d) Confusion matrix results for dynamic gesture recognition task without motion object extraction system. e) Confusion matrix results for dynamic gesture recognition task with motion object extraction system.

information also encompasses numerous extraneous static back-drop elements, unrelated objects, and potential noise interference. In addition to significantly increasing the computing load and complexity of data processing, the presence of redundant information also introduces errors and confusion into the action recognition process, which compromises the accuracy and dependability of the final recognition. The pre-processing systems for motion detection can make this problem better solved. It can effectively separate and extract the dynamic information of the moving objects from the original video input. In the gesture recognition task, the dynamic gesture dataset is provided by Guthub and processed by the preprocessing system. The processed image frames retained only three types of motion information: scissors, rock, and fabric. These image frames were subsequently fed into a trained convolutional neural network (CNN) to recognize the gesture categories (Figure 5c). The confusion matrix in Figure 5d,e compares the identification results of the CNN with and without the motion object detection system. The results demonstrate that the utilization of the motion detection system for target extraction enhances the recognition accuracy of the network from the initial 84.7% to 98.1%. A strong technical

solution to accomplish accurate and efficient action recognition is provided by the effective combination of CNN and motion object detection systems, particularly in intelligent surveillance, autonomous driving, and other scenarios requiring real-time processing of large amounts of video data.

3. Conclusion

Ultimately, we have fabricated an organic ambipolar transistor with excellent balanced bipolar characteristics using spin-coating and thermal evaporation techniques. Under the influence of light pulses and gate voltage, it demonstrates both excitatory and inhibitory photosynaptic behaviors. By constructing two 20×20 OFET arrays to replicate the parallel processing mechanism of *Drosophila*, the distinction between moving objects and background information was enhanced for the purpose of recognizing motion direction and detecting motion. Based on this foundation, systems for recognizing motion direction and a system for recognizing dynamic gestures were effectively constructed, achieving recognition accuracies of 94.8% and 98.1%, respectively. This accomplishment not only showcases

the significant capabilities of organic ambipolar transistors in the realm of bionic vision but also offers novel insights for the future advancement of intelligent perception and human-computer interaction systems.

4. Experimental Section

Materials Availability: All of the materials were used without further purification: Pentacene was purchased from Tokyo Chemical Industry (TCI), PbS QDs were selected to have a maximum emission peak around 950 nm, and C₆₀ was chosen to have a purity of 99.9%. Both materials were purchased from Nanjing MKNANO Tech. Co.

Device Fabrication: The p-type SiO₂ (300 nm) was used as a substrate and ultrasonically cleaned with deionized water, acetone, and isopropanol for 15 min, respectively, treated in UV/ozone for 15 min. 2 mg mL⁻¹ of PbS QDs solution (solvent: toluene) was configured, and the solution was spin-coated onto the substrate (2000 rpm, 50 s) and annealed at 100 °C for 15 min in the nitrogen filled glove box. Subsequently, to form the heterojunction structure, the C₆₀ (350 °C) and pentacene (170 °C) were sequentially deposited on QDs films layer by thermal vacuum evaporation in a vacuum of 1×10^{-4} Pa at a deposition rate of 0.2 Å s⁻¹. Ultimately, Au source/drain electrodes with a 50 µm channel width and 50 nm thickness were formed via thermal evaporation utilizing a mask plate in a vacuum of 1×10^{-4} Pa at a deposition rate of 0.1 Å s⁻¹. Similar steps were taken to construct the 20 × 20 arrays, but to prevent direct contact between the electrodes, a layer of hafnium oxide (HfO₂) was added as an insulating layer by magnetron sputtering during the electrode preparation.

Instrumentation: The electrical and optical properties of PbS/C₆₀/pentacene device, including I–V characteristics, I–T characteristics, and dynamic behavior under optical pulse stimulation, were carried out using a probe station equipped with a Keithley B2902A precision source/measure system. A combination equipment of light source equipment (980 nm laser and 458/519/637 nm commercial LED) and signal generator (Gwinstel AFG-2225) was used in the measurement of synaptic characteristics. Power density of NIR light was measured by a power meter (Thorlabs S121C). All of the above testing were performed in a glovebox with a nitrogen atmosphere at room temperature.

Characterization: The surface morphologies and surface potentials of thin films were investigated using a commercial AFM (Bruker Dimension Icon) in a nitrogen atmosphere. The absorption characteristics of the thin films were measured using an ultraviolet–visible (UV–vis) spectrophotometer (Cary60, Agilent). The distribution of PbS QDs was characterized by TEM (Titan Cube Themis G2300, FEI). The cross-sectional image of the device was characterized through a field emission SEM (FEI Scios, Thermo Fisher).

Orientation Recognition Tasks: Each pixel in a 20 × 20 image frame over four time periods is converted to a binary state of “0” or “1” represented by a 458 nm light pulse, and the “1” and “0” light intensities were set to 28.8 and 0 µW cm⁻², respectively. The pulse width of the 458 nm signal for each pixel was 0.2 s, and the pulse interval was 0.2 s. The response current was also measured by applying a constant drain voltage ($V_{ds} = -3$ V) and gate voltage ($V_g = -15$ V and $V_g = 5$ V) to the device. Sixteen different time series data (“0000”–“1111”) are input into the device, and the I_{ds} of the current moment is obtained as the reservoir state after the fourth pulse input. For the orientation recognition task, 400 sets of pixel data are converted into stored state values for training in an ANN network, and classification is performed in the output layer species. The training of the weights was implemented in MATLAB with the activation of the softmax function. A cross-entropy loss function was defined to evaluate the difference between the predicted and target values and gradient descent was used to iterate the weights of the readout layer. In each case, the training set comprised 1000 images (8000 images in total), while the test set consisted of 300 samples (2400 images in total). The learning rate of the network was set at 0.001.

Dynamic Gesture Classification Tasks: The dynamic gesture dataset, which has been made open-source on GitHub (https://github.com/wangsc1912/rc_pndi), is used. First, the video data are preprocessed and

decomposed into a series of 5000 consecutive frames containing only dynamic motion objects by applying the motion object detection technique. Thereafter, 368 image frames of each are randomly selected as the test data. The construction of the CNN is based on the combination of convolutional operations and the ReLU activation function. This enables the CNN to learn and construct an efficient mapping from the raw pixels to the high-level semantic features. Concurrently, the Adam optimizer is employed to regulate the network training process, with the objective of accelerating convergence and improving training efficiency. In the training phase, the weight parameters of the network are optimized by the back-propagation algorithm and the cross-entropy loss function in an iterative process.

Supporting Information

Supporting Information is available from the Wiley Online Library or from the author.

Acknowledgements

T.X. and Y.-B.L. contributed equally to this work. This research was supported by the NSFC Program (Grant Nos. 62122055, 62074104), Guangdong Basic and Applied Basic Research Foundation (Grant No. 2024B1515040002) and RSC Researcher Collaborations Grant (Grant No. C23-2422436283).

Conflict of Interest

The authors declare no conflict of interest.

Data Availability Statement

The data that support the findings of this study are available from the corresponding author upon reasonable request.

Keywords

ambipolar transistor, Drosophila visual system, motion detection, organic electronics, synapse

Received: August 22, 2024

Revised: October 21, 2024

Published online:

- [1] X. Liu, S. Dai, W. Zhao, J. Zhang, Z. Guo, Y. Wu, Y. Xu, T. Sun, L. Li, P. Guo, J. Yang, H. Hu, J. Zhou, P. Zhou, J. Huang, *Adv. Mater.* **2024**, 36, 2312473.
- [2] Y. Cai, F. Wang, X. Wang, S. Li, Y. Wang, J. Yang, T. Yan, X. Zhan, F. Wang, R. Cheng, J. He, Z. Wang, *Adv. Funct. Mater.* **2023**, 33, 2212917.
- [3] S. Zhu, T. Xie, Z. Lv, Y.-B. Leng, Y.-Q. Zhang, R. Xu, J. Qin, Y. Zhou, V. A. L. Roy, S.-T. Han, *Adv. Mater.* **2024**, 36, 2301986.
- [4] L. Mennel, J. Symonowicz, S. Wachter, D. Polyushkin, A. Molina-Mendoza, T. Mueller, *Nature*. **2020**, 579, 62.
- [5] K. Wang, Y. Liao, W. Li, J. Li, H. Su, R. Chen, J. H. Park, Y. Zhang, X. Zhou, C. Wu, Z. Liu, T. Guo, T. W. Kim, *Nat. Commun.* **2024**, 15, 3505.
- [6] Y. Wang, F. Wang, Z. Wang, J. Wang, J. Yang, Y. Yao, N. Li, M. G. Sendeku, X. Zhan, C. Shan, J. He, *Nano Res.* **2021**, 14, 4328.
- [7] G. K. Gupta, I.-J. Kim, Y. Park, M.-K. Kim, J.-S. Lee, *ACS Appl. Mater. Interfaces*. **2023**, 15, 18055.

- [8] I.-J. Kim, J.-S. Lee, *Adv. Mater.* **2023**, 35, 2206864.
- [9] S. Yoo, Y. Park, Z. Wang, Y. Wu, S. Medepalli, W. Thio, W. D. Lu, *Adv. Intell. Syst.* **2022**, 4, 2200179.
- [10] G. Orchard, R. Etienne-Cummings, *Proc. IEEE* **2014**, 102, 1520.
- [11] F. Aguirre, A. Sebastian, M. L. Gallo, W. Song, T. Wang, J. J. Yang, W. Lu, M.-F. Chang, D. Ielmini, Y. Yang, A. Mehon, A. Kenyon, M. A. Villena, J. B. Roldán, Y. Wu, H.-H. Hsu, N. Raghavan, J. Suñé, E. Miranda, A. Eltawil, G. Setti, K. Smagulova, K. N. Salama, O. Krestinskaya, X. Yan, K.-W. Ang, S. Jain, S. Li, O. Alharbi, S. Pazos, et al., *Nat. Commun.* **2024**, 15, 1974.
- [12] N. Lin, J. Chen, R. Zhao, Y. He, K. Wong, Q. Qiu, Z. Wang, J. J. Yang, *APL Mach. Learn.* **2024**, 2, 010901.
- [13] J.-J. Kim, H. Liu, A. O. Ashtiani, H. Jiang, *Rep. Prog. Phys.* **2020**, 83, 047101.
- [14] Y. Yang, C. Pan, Y. Li, X. Yangdong, P. Wang, Z.-A. Li, S. Wang, W. Yu, G. Liu, B. Cheng, Z. Di, S.-J. Liang, F. Miao, *Nat. Electron.* **2024**, 7, 225.
- [15] F. Zhou, Y. Chai, *Nat. Electron.* **2020**, 3, 664.
- [16] L. Jiang, B. Wang, F. Ni, W. Xu, X. Wang, L. Zheng, L. Qiu, *ACS Photonics* **2024**, 11, 3187.
- [17] Y. Ni, J. Liu, H. Han, Q. Yu, L. Yang, Z. Xu, C. Jiang, L. Liu, W. Xu, *Nat. Commun.* **2024**, 15, 3454.
- [18] I. A. Meinertzhagen, S. D. O'Neil, *J. Comp. Neurol.* **1991**, 305, 232.
- [19] L. C. Kogos, Y. Li, J. Liu, Y. Li, L. Tian, R. Paiella, *Nat. Commun.* **2020**, 11, 1637.
- [20] Z. Deng, F. Chen, Q. Yang, H. Bian, G. Du, J. Yong, C. Shan, X. Hou, *Adv. Funct. Mater.* **2016**, 26, 1995.
- [21] D. Floreano, R. Pericet-Camara, S. Viollet, F. Ruffier, A. Brückner, R. Leitel, W. Buss, M. Menouni, F. Expert, R. Juston, M. K. Dobrzynski, G. L'Eplattenier, F. Recktenwald, H. A. Mallot, N. Franceschini, *Proc. Natl. Acad. Sci. USA* **2013**, 110, 9267.
- [22] D. A. Clark, J. B. Demb, *Curr. Biol.* **2016**, 26, R1062.
- [23] E. Salazar-Gatzimas, M. Agrochao, J. E. Fitzgerald, D. A. Clark, *Curr. Biol.* **2018**, 28, 3748.
- [24] J. Chen, H. B. Mandel, J. E. Fitzgerald, D. A. Clark, *eLife* **2019**, 8, e47579.
- [25] M. Joesch, B. Schnell, S. V. Raghu, D. F. Reiff, A. Borst, *Nature* **2010**, 468, 300.
- [26] Z. Huang, S. Kunes, *Development* **1998**, 125, 3753.
- [27] J. R. Sanes, S. L. Zipursky, *Neuron* **2010**, 66, 15.
- [28] M. P. Bostock, A. R. Prasad, A. Donoghue, V. M. Fernandes, *eLife* **2022**, 11, e78093.
- [29] T. Erclik, X. Li, M. Courgeon, C. Bertet, Z. Chen, R. Baumert, J. Ng, C. Koo, U. Arain, R. Behnia, A. Del Valle Rodriguez, L. Senderowicz, N. Negre, K. P. White, C. Desplan, *Nature* **2017**, 541, 365.
- [30] C. Schnaitmann, V. Haikala, E. Abraham, V. Oberhauser, T. Thestrup, O. Griesbeck, D. F. Reiff, *Cell* **2018**, 172, 318.
- [31] H. Wang, J. Peng, S. Yue, *IEEE Trans. Cybern.* **2020**, 50, 1541.
- [32] S.-Y. Takemura, Z. Lu, I. A. Meinertzhagen, *J. Comp. Neurol.* **2008**, 509, 493.
- [33] N. Neric, C. Desplan, *Curr. Top. Dev. Biol.* **2016**, 116, 247.
- [34] J. M. Ache, J. Polsky, S. Alghailani, R. Parekh, P. Breads, M. Y. Peek, D. D. Bock, C. R. von Reyn, G. M. Card, *Curr. Biol.* **2019**, 29, 1073.
- [35] K. Shinomiya, A. Nern, I. A. Meinertzhagen, S. M. Plaza, M. B. Reiser, *Curr. Biol.* **2022**, 32, 3529.
- [36] N. C. Klapoetke, A. Nern, M. Y. Peek, E. M. Rogers, P. Breads, G. M. Rubin, M. B. Reiser, G. M. Card, *Nature* **2017**, 551, 237.
- [37] E. Salazar-Gatzimas, J. Chen, M. S. Creamer, O. Mano, H. B. Mandel, C. A. Matulis, J. Pottackal, D. A. Clark, *Neuron* **2016**, 92, 227.
- [38] H. Apitz, I. Salecker, *Nat. Commun.* **2018**, 9, 2295.
- [39] F. Pinto-Teixeira, C. Koo, A. M. Rossi, N. Neric, C. Bertet, X. Li, A. Del-Valle-Rodriguez, C. Desplan, *Cell* **2018**, 173, 485.
- [40] M. Kumar, J. Lim, S. Kim, H. Seo, *ACS Nano* **2020**, 14, 14108.
- [41] X. Geng, L. Hu, F. Zhuge, X. Wei, *Adv. Intell. Syst.* **2022**, 4, 2200019.
- [42] T. Jiang, Y. Wang, Y. Zheng, L. Wang, X. He, L. Li, Y. Deng, H. Dong, H. Tian, Y. Geng, L. Xie, Y. Lei, H. Ling, D. Ji, W. Hu, *Nat. Commun.* **2023**, 14, 2281.
- [43] C. Jo, J. Kim, J. Y. Kwak, S. M. Kwon, J. B. Park, J. Kim, G. Park, M. Kim, Y. Kim, S. K. Park, *Adv. Mater.* **2022**, 34, 2108979.
- [44] Z. He, H. Shen, D. Ye, L. Xiang, W. Zhao, J. Ding, F. Zhang, C. Di, D. Zhu, *Nat. Electron.* **2021**, 4, 522.
- [45] Q. Wu, B. Dang, C. Lu, G. Xu, G. Yang, J. Wang, X. Chuai, N. Lu, D. Geng, H. Wang, L. Li, *Nano Lett.* **2020**, 20, 8015.
- [46] M. Hu, J. Yu, Y. Chen, S. Wang, B. Dong, H. Wang, Y. He, Y. Ma, F. Zhuge, T. Zhai, *Mater. Horiz.* **2022**, 9, 2335.
- [47] J.-K. Han, D.-M. Geum, M.-W. Lee, J.-M. Yu, S. K. Kim, S. Kim, Y.-K. Choi, *Nano Lett.* **2020**, 20, 8781.
- [48] A. Leonhardt, G. Ammer, M. Meier, E. Serbe, A. Bahl, A. Borst, *Nat. Neurosci.* **2016**, 19, 706.
- [49] C.-Y. Wang, S.-J. Liang, S. Wang, P. Wang, Z. Li, Z. Wang, A. Gao, C. Pan, C. Liu, J. Liu, H. Yang, X. Liu, W. Song, C. Wang, B. Cheng, X. Wang, K. Chen, Z. Wang, K. Watanabe, T. Taniguchi, J. J. Yang, F. Miao, *Sci. Adv.* **2020**, 6, eaba6173.
- [50] Y. Ren, X. Yang, L. Zhou, J.-Y. Mao, S.-T. Han, Y. Zhou, *Adv. Funct. Mater.* **2019**, 29, 1902105.
- [51] W. Hu, Z. Sheng, X. Hou, H. Chen, Z. Zhang, D. W. Zhang, P. Zhou, *Small Methods* **2021**, 5, 2000837.
- [52] X. Zhu, C. Gao, Y. Ren, X. Zhang, E. Li, C. Wang, F. Yang, J. Wu, W. Hu, H. Chen, *Adv. Mater.* **2023**, 35, 2301468.
- [53] L. Zhou, J.-Y. Mao, Y. Ren, J.-Q. Yang, S.-R. Zhang, Y. Zhou, Q. Liao, Y.-J. Zeng, H. Shan, Z. Xu, J. Fu, Y. Wang, X. Chen, Z. Lv, S.-T. Han, V. A. L. Roy, *Small* **2018**, 14, 1800288.
- [54] H. Jörntell, C. Hansel, *Neuron* **2006**, 52, 227.
- [55] Y. LeCun, Y. Bengio, G. Hinton, *Nature* **2015**, 521, 436.
- [56] D. E. Rumelhart, G. E. Hinton, R. J. Williams, *Nature* **1986**, 323, 533.
- [57] J. K. Eshraghian, M. Ward, E. O. Neftci, X. Wang, G. Lenz, G. Dwivedi, M. Bennamoun, D. S. Jeong, W. D. Lu, *Proc. IEEE* **2023**, 111, 1016.
- [58] L. Guo, J. Han, J. Wang, *J. Mater. Chem. C* **2024**, 12, 1233.
- [59] X. Shi, Y. Xu, W. Liu, C. Jin, S. Wang, J. Sun, J. Yang, *Adv. Funct. Mater.* **2024**, 34, 2401534.
- [60] S. Z. Bisri, C. Piliago, J. Gao, M. A. Loi, *Adv. Mater.* **2014**, 26, 1176.
- [61] J. Song, H. Liu, Z. Zhao, P. Lin, F. Yan, *Adv. Mater.* **2024**, 36, 2300034.
- [62] Y. Ran, W. Lu, X. Wang, Z. Qin, X. Qin, G. Lu, Z. Hu, Y. Zhu, L. Bu, G. Lu, *Mater. Horiz.* **2023**, 10, 4438.
- [63] Y. Wang, R. Zhou, H. Cong, G. Chen, Y. Ma, S. Xin, D. Ge, Y. Qin, S. Ramakrishna, X. Liu, F. Wang, *Adv. Fiber Mater.* **2023**, 5, 1919.
- [64] S. Lan, J. Zhong, J. Chen, W. He, L. He, R. Yu, G. Chen, H. Chen, *J. Mater. Chem. C* **2021**, 9, 3412.
- [65] Y. Gong, P. Xie, X. Xing, Z. Lv, T. Xie, S. Zhu, H.-H. Hsu, Y. Zhou, S.-T. Han, *Adv. Funct. Mater.* **2023**, 33, 2303539.
- [66] Y. Sun, Y. Ding, D. Xie, J. Xu, M. Sun, P. Yang, Y. Zhang, *Adv. Opt. Mater.* **2021**, 9, 2002232.
- [67] C. Zhang, M. Zhang, F. Lin, G. Zhao, Z. Wei, Y. Ni, J. Li, H. Yu, X. Zhao, Y. Tong, Q. Tang, Y. Liu, *Adv. Electron. Mater.* **2024**, 10, 2300878.
- [68] K. Eguchi, M. M. Matsushita, K. Awaga, *J. Phys. Chem. C* **2018**, 122, 26054.
- [69] L. Liu, N. Xu, Y. Zhang, P. Zhao, H. Chen, S. Deng, *Adv. Funct. Mater.* **2019**, 29, 1807893.
- [70] C. Liu, H. Peng, K. Wang, C. Wei, Z. Wang, X. Gong, *Nano Energy* **2016**, 30, 27.
- [71] M. Zhang, Z. Chi, G. Wang, Z. Fan, H. Wu, P. Yang, J. Yang, P. Yan, Z. Sun, *Adv. Mater.* **2022**, 34, 2205679.
- [72] J. Zhang, P. Guo, Z. Guo, L. Li, T. Sun, D. Liu, L. Tian, G. Zu, L. Xiong, J. Zhang, J. Huang, *Adv. Funct. Mater.* **2023**, 33, 2302885.
- [73] R. R. de Ruyter van Steveninck, S. B. Laughlin, *Nature* **1996**, 379, 642.
- [74] A. Arenz, M. S. Drews, F. G. Richter, G. Ammer, A. Borst, *Curr. Biol.* **2017**, 27, 929.

- [75] B. A. Badwan, M. S. Creamer, J. A. Zavatone-Veth, D. A. Clark, *Nat. Neurosci.* **2019**, 22, 1318.
- [76] S. Takemura, T. Karuppudurai, C.-Y. Ting, Z. Lu, C.-H. Lee, I. A. Meinertzhagen, *Curr. Biol.* **2011**, 21, 2077.
- [77] H. Eichner, M. Joesch, B. Schnell, D. F. Reiff, A. Borst, *Neuron.* **2011**, 70, 1155.
- [78] E. L. Barnhart, I. E. Wang, H. Wei, C. Desplan, T. R. Clandinin, *Neuron.* **2018**, 100, 229.
- [79] J. Chen, Z. Zhou, B. J. Kim, Y. Zhou, Z. Wang, T. Wan, J. Yan, J. Kang, J.-H. Ahn, Y. Chai, *Nat. Nanotechnol.* **2023**, 18, 882.
- [80] T. Chen, S. Lu, *IEEE Trans. Circuits Syst. Video Technol.* **2017**, 27, 2333.
- [81] Y. Wu, W. Deng, X. Chen, J. Li, S. Li, Y. Zhang, *Sci. China Inf. Sci.* **2023**, 66, 162401.
- [82] H. Wang, J. Peng, X. Zheng, S. Yue, *IEEE Trans. Neural Networks Learn. Syst.* **2020**, 31, 839.